Energy & Environmental Science

ROYAL SOCIETY OF CHEMISTRY

PAPER

View Article Online
View Journal | View Issue

Cite this: *Energy Environ. Sci.*, 2025, **18**, 3269

Damp-heat stable and efficient perovskite solar cells and mini-modules with a *t*BP-free hole-transporting layer†

Yun Seop Shin, ‡[ab] Jaehwi Lee,‡[b] Dong Gyu Lee,‡[c] Ji Won Song, [a] Jongdeuk Seo, [b] Jina Roe,[b] Min Jung Sung,[a] Sujung Park,[d] Gwang Yong Shin,[c] Jiwoo Yeop,[b] Dongmin Lee,[a] Chang Hyeon Yoon,[a] Minseong Kim,[a] Jung Geon Son,[b] Gi-Hwan Kim, [c] Shinuk Cho, [d] Jin Young Kim, [ab] Tae Kyung Lee *[ce] and Dong Suk Kim *[ab]

Received 3rd December 2024,
Accepted 13th February 2025

DOI: 10.1039/d4ee05699j

rsc.li/ees

In spiro-OMeTAD-based hole-transporting layer (HTL) protocols, 4-*tert*-butylpyridine (*t*BP) is an indispensable component; however, its inclusion leads to substantial detrimental effects, hindering thermal stability. Here, a *t*BP-free spiro-OMeTAD approach was successfully devised by substituting ethylene carbonate (EC) electrolyte for *t*BP. The electronegative carbonyl functionality led to the formation of a solvation complex with Li^+ ions, addressing the solubility concern of lithium bis(trifluoromethanesulfonyl)imide (LiTFSI) in chlorobenzene even without *t*BP. The liberated $TFSI^-$ ions facilitate the stabilization of a larger population of spiro-OMeTAD$^{\bullet+}$ radicals, thereby enabling efficient p-doping. The EC-incorporated HTL achieved a maximum power conversion efficiency (PCE) of 25.56% (certified 25.51%). In scaled-up applications, perovskite solar mini-modules with aperture areas of 25 and 100 cm^2 demonstrated PCEs of 23.22% and 22.14%, respectively. The elevated glass transition temperature and robustly sequestered Li^+ ions endow the devices with resilience against damp-heat conditions (85 °C/85% RH) for 1000 hours. Our findings signify a crucial leap towards commercialization by addressing thermal stability issues.

Broader context

The π-conjugated small molecule spiro-OMeTAD stands as a benchmark hole-transporting layer (HTL) used for achieving high efficiency in n–i–p perovskite solar cells. In a conventional p-doping mechanism, the 4-*tert*-butylpyridine (*t*BP) additive plays a pivotal role by enhancing the solubility of lithium bis(trifluoromethanesulfonyl)imide (LiTFSI) in chlorobenzene (CB), refining the morphological uniformity of spiro-OMeTAD films and liberating $TFSI^-$ ions to stabilize p-doped radicals. However, the incorporation of *t*BP leads to significant drawbacks, including a reduction in glass transition temperature (T_g), de-doping of hole conductors, and perovskite degradation, necessitating the development of a *t*BP-free HTL protocol to ensure both high performance and long-term stability. This study pioneers an alternative doping strategy that substitutes *t*BP with ethylene carbonate (EC) electrolyte by leveraging its solvating capability for Li^+ ions through its electronegative carbonyl functionality. The formation of a Li^+:EC solvating complex not only enhances the solubility of LiTFSI in CB but also promotes the formation of uniform spiro-OMeTAD films, eliminating pinholes and dopant aggregation, even in the absence of *t*BP. Consequently, the EC-integrated HTL achieved record-breaking efficiency among *t*BP-free HTL systems and demonstrated impressive scalability for larger-area perovskite solar modules. Furthermore, the elevated T_g and resilient Li^+:EC coordination imparted exceptional reliability under harsh damp-heat conditions (85 °C/85% RH).

[a] *Graduate School of Carbon Neutrality, Ulsan National Institute of Science and Technology (UNIST), Ulsan 44919, Republic of Korea. E-mail: kimds@unist.ac.kr*
[b] *School of Energy and Chemical Engineering, Ulsan National Institute of Science and Technology (UNIST), Ulsan 44919, Republic of Korea*
[c] *Department of Materials Engineering and Convergence Technology, Gyeongsang National University (GNU), Jinju 52828, Republic of Korea. E-mail: tklee8865@gnu.ac.kr*
[d] *Department of Physics and Energy Harvest Storage Research Centre, University of Ulsan, Ulsan 44610, Republic of Korea*
[e] *School of Materials Science and Engineering, Gyeongsang National University (GNU), Jinju 52828, Republic of Korea*

† Electronic supplementary information (ESI) available. See DOI: https://doi.org/10.1039/d4ee05699j

‡ These authors contributed equally to this work.

Introduction

Spiro-OMeTAD, a π-conjugated small molecule, has emerged as an ideal hole conductor and a definitive benchmark for high-efficiency n–i–p perovskite solar cells (PSCs).[1–3] However, its inherently limited electrical properties necessitate oxygen-assisted p-doping,[4,5] enhanced by the inclusion of 4-*tert*-butylpyridine (*t*BP) and lithium bis(trifluoromethanesulfonyl)imide (LiTFSI) as p-dopants. As a conventional doping paradigm, the doping agent LiTFSI enables the formation of spiro-OMeTAD$^{\bullet+}$TFSI$^-$ radicals,[6] while *t*BP enhances morphological homogeneity.[7] Despite significant efficiency gains, these dopants compromise long-term light and thermal stability, posing challenges to the commercialization of PSCs. Specifically, *t*BP, while critical for influencing the morphological properties of spiro-OMeTAD, reduces the glass transition temperature (T_g),[8] induces de-doping of the hole conductor,[9] and accelerates perovskite degradation.[10] Our prior work demonstrated that these issues could be mitigated by judiciously optimizing the molar ratio of *t*BP to LiTFSI to form a robust 1 : 1 *t*BP : Li$^+$ complex,[11] yielding exceptional improvements in both efficiency and long-term stability. Nevertheless, a sustainable path forward necessitates eliminating the use of *t*BP, requiring alternative strategies that concurrently address lingering solubility challenges of LiTFSI.

The actual doping mechanism of spiro-OMeTAD is designed to attain TFSI-stabilized radical cations.[12,13] Consequently, the generation of p-doped radicals in spiro-OMeTAD$^{\bullet+}$TFSI$^-$ necessitates the dissociation of TFSI$^-$ ions from the LiTFSI, a critical process for stabilizing spiro-OMeTAD$^{\bullet+}$. However, in non-polar solvents, this dissociation remains formidable,[14] underscoring the need for a strategic formation of a solvation complex with Li$^+$ ions. Ethylene carbonate (EC) is commonly used as a prototypical electrolyte solvent in Li-ion batteries,[15,16] where Li$^+$ ions typically coordinate with electronegative carbonyl oxygen atoms, forming a solvation complex.[17,18] Building on this point, this property inspired us to explore alternatives to *t*BP.

Here, we propose an innovative approach for realizing a *t*BP-free hole-transporting layer (HTL) protocol by incorporating EC as a replacement for *t*BP. The solvating ability of EC enables LiTFSI to enhance its solubility in chlorobenzene (CB) in the absence of *t*BP, promoting the morphological uniformity of the spiro-OMeTAD film, devoid of pinholes and aggregation. The improved solubility of LiTFSI facilitates the formation of a greater density of p-doped radicals, significantly enhancing the electrical properties. Additionally, the incorporation of EC not only elevates the T_g, guaranteeing long-term thermal stability, but also obstructs ion migration within the device by forming coordination complexes with Li$^+$ ions. Using the proposed approach, PSCs achieved an outstanding maximum power conversion efficiency (PCE) of 25.56% (certified 25.51%), the highest efficiency recorded for *t*BP-free HTL systems. More encouragingly, with respect to large-area applications, perovskite solar mini-modules (PSMs) featuring aperture areas of 25 and 100 cm^2 attained impressive PCEs of 23.22% and 22.14%, respectively. Additionally, the elevated T_g and the formation of a robust Li$^+$:EC complex endow the devices with the ability to endure the damp-heat conditions (85 °C/85% relative humidity [RH]), demonstrating reliabilities of 85% and 87% over durations of 1000 and 700 hours for PSCs and PSMs, respectively.

Results and discussion

The incorporation of EC as an additive was meticulously engineered to replace *t*BP in the spiro-OMeTAD HTL framework, enabling the development of a *t*BP-free HTL system. This substitution facilitates the dissolution of LiTFSI in the CB solvent by promoting the formation of solvating complexes with Li$^+$ ions from LiTFSI. To ascertain the chemical interactions between Li$^+$ ions and EC, nuclear magnetic resonance (NMR) spectroscopy, including ^{7}Li- and ^{1}H-NMR, was conducted on the LiTFSI and EC mixture. Upon introducing EC, the ^{7}Li-NMR signal of LiTFSI, originally detected at 0.079 ppm, shifted toward a higher ppm of 0.124 ppm (Fig. 1a), while the ^{1}H-NMR signal of EC (denoted as H_a in Fig. 1b) slightly shifted from 4.53 ppm to 4.56 ppm following LiTFSI addition. In pursuit of a more comprehensive understanding of the atomic-level interactions between LiTFSI and EC, two-dimensional (2D) ^{7}Li–^{1}H heteronuclear Overhauser enhancement spectroscopy (HOESY) measurements were performed. The emergence of off-diagonal peaks signifies atomic-scale proximity between the two species, offering definitive evidence of the interaction between Li$^+$ ions and EC[19,20] (Fig. 1c). Furthermore, Fourier transform infrared spectroscopy (FTIR) measurements were conducted to pinpoint the specific sites on the EC molecule (Fig. 1d). Two prominent peaks, corresponding to the stretching vibrations of the carbonyl group (C═O) in EC,[21,22] appeared at 1796 and 1769 cm^{-1} and shifted to higher wavenumbers of 1804 and 1774 cm^{-1}, respectively, upon LiTFSI addition. Consequently, these spectroscopic results unambiguously delineate the binding mechanism, whereby EC selectively engages with Li$^+$ ions in the mixture.

To gain an in-depth understanding of the atomic-level binding characteristics between Li$^+$ ions and EC molecules, density functional theory (DFT) calculations were performed. The electrostatic potential isosurface of the EC molecule revealed that the carbonyl group serves as the predominant binding site for Li$^+$ ions due to strong electrostatic interactions (Fig. S1, ESI†). Building on this, we conducted a detailed investigation of the binding energies between Li$^+$ ions and EC molecules as the number of EC molecules increased. The complexes formed between Li$^+$ ions and EC molecules exhibited thermodynamically favourable interactions, with increasing binding strength as the number of EC molecules decreased (Fig. 1e and Fig. S2, ESI†). To further probe the solvation dynamics of Li$^+$ ions and EC molecules, molecular dynamics (MD) simulations were conducted (Fig. S3 and Table S1, ESI†). The solvation free energy of Li$^+$ ions became increasingly thermodynamically favourable with the addition of EC compared to the control case (Fig. 1f), indicating that EC molecules can interact with and solvate Li$^+$ ions. Upon introducing EC, the coordination number of Li$^+$ and TFSI$^-$ ions, derived from radial distribution functions (RDF), was reduced, attributable to the selective coordination of a single

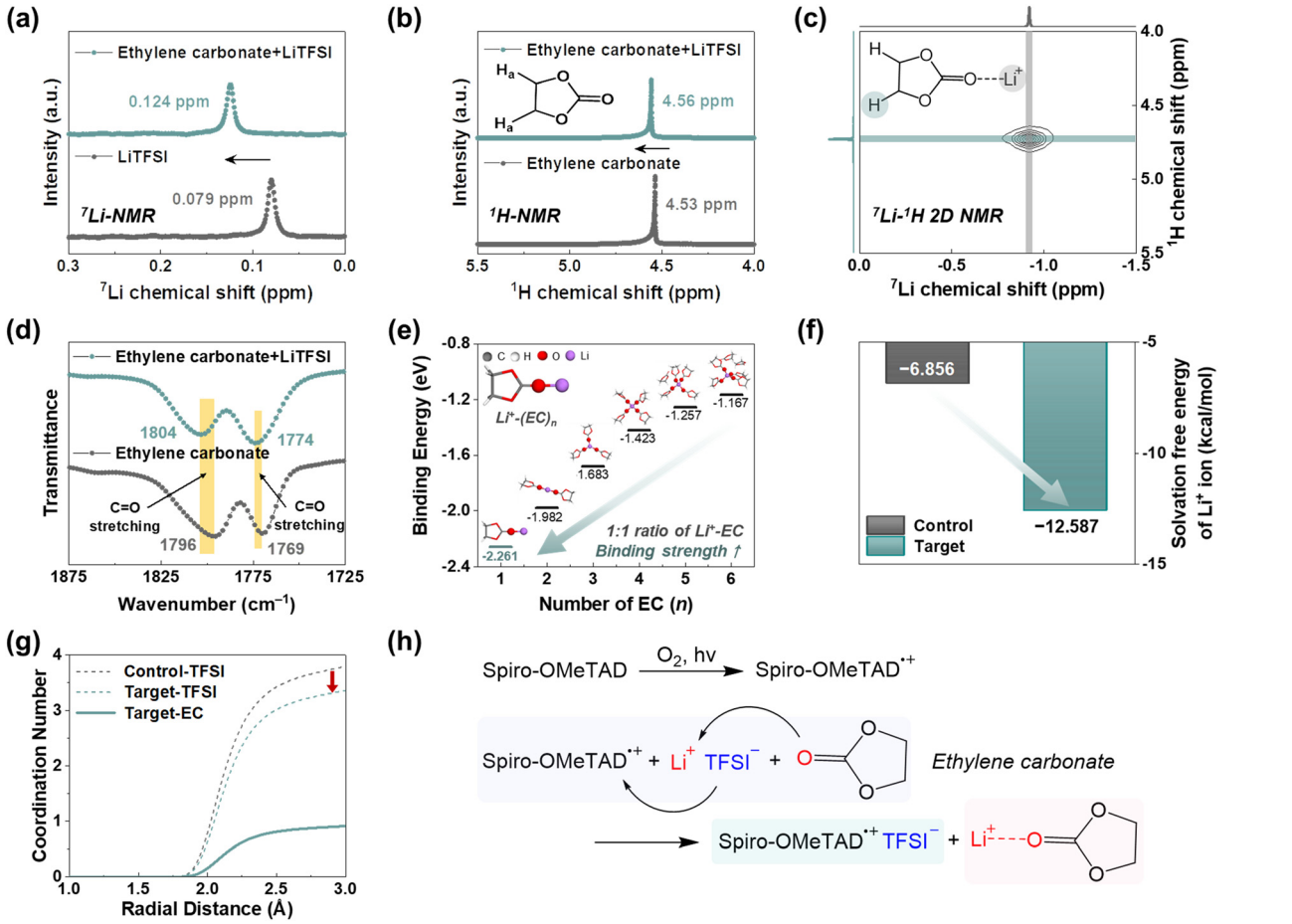

Fig. 1 Doping mechanism of EC-incorporated spiro-OMeTAD HTLs. (a) ^{7}Li-NMR spectra of LiTFSI and its mixture with EC. (b) ^{1}H-NMR spectra of EC and its mixture with LiTFSI. (c) 2D ^{7}Li–^{1}H HOESY spectra of the LiTFSI and EC mixture. (d) FTIR spectra of EC and its mixture with EC. (e) Binding energies of the Li^+ ion with $(EC)_n$, where n denotes the number of EC molecules. (f) Solvation free energies of the Li^+ ion under the control and target conditions. (g) Coordination numbers of the Li^+ ion with the $TFSI^-$ ion (oxygen atom) and EC (oxygen atom in the carbonyl group) under the control and target conditions. (h) Illustration of the doping mechanism of EC-incorporated spiro-OMeTAD HTLs.

EC molecule under the target conditions (Fig. 1g and Fig. S4, ESI†). Notably, the binding energy between the Li^+ and $TFSI^-$ ions diminished in the presence of EC molecules (Fig. S5, ESI†), demonstrating that EC alters the solvation structure surrounding Li^+ ions and simultaneously weakens their binding strength with $TFSI^-$ ions. Furthermore, the remaining $TFSI^-$ ions, promoted by EC molecules, formed thermodynamically favourable interactions with spiro-OMeTAD$^{\bullet+}$ radicals, enhancing doping efficiency (Fig. S6, ESI†). As summarized in Fig. 1h, EC molecules selectively bind to Li^+ ions in the LiTFSI precursor, facilitating its dissolution in the non-polar CB solvent.[23] This reaction prevents ion migration by sequestering Li^+ ions, while the liberated $TFSI^-$ ions proficiently stabilize the spiro-OMeTAD$^{\bullet+}$ radicals, thus improving the overall doping process.

Typically, the LiTFSI p-dopant has been deployed by dissolving it in the polar solvent acetonitrile, necessitating *t*BP to enhance its miscibility with the non-polar CB solvent. Expanding on the in-depth analysis delineated in Fig. 1, the solvation complex between Li^+ ions and EC molecules facilitates LiTFSI dissolution in CB, obviating the necessity for *t*BP (Fig. 2a). This solvation behaviour accelerates the p-doping process, evident from the colour transition of the spiro-OMeTAD solution to reddish upon adding LiTFSI with EC (Fig. 2b). A prominent absorption peak at 520 nm, characteristic of spiro-OMeTAD$^{\bullet+}$$TFSI^-$ radicals,[24,25] was observed immediately after adding LiTFSI. This indicates that spiro-OMeTAD$^{\bullet+}$$TFSI^-$ radicals are rapidly formed upon stabilization by dissociated $TFSI^-$ ions,[26,27] further corroborated by an intense electron spin resonance (ESR) signal (Fig. 2c). Under one hour of light illumination, substantial p-doping occurs, leading to pronounced changes in the electrical properties of spiro-OMeTAD, contingent upon the presence of EC (Fig. 2d). Without *t*BP, the limited solubility of LiTFSI yielded an electrical conductivity of just 2.79×10^{-4} S cm^{-1} for the spiro-OMeTAD film without EC (denoted as control; 0 μL of *t*BP and 3 μL of LiTFSI in 1 mL of CB). Increasing LiTFSI beyond 3 μL caused considerable morphological deformation of the spiro-OMeTAD film with numerous pinholes forming due to the miscibility mismatch[28] (Fig. S7, ESI†). This phenomenon was also correlated with a decline in electrical conductivity in the 5 μL and 7 μL of LiTFSI (Fig. S8, ESI†). To explore the correlation between the solvating behaviour of EC and the electrical properties of spiro-OMeTAD, we conducted an investigation

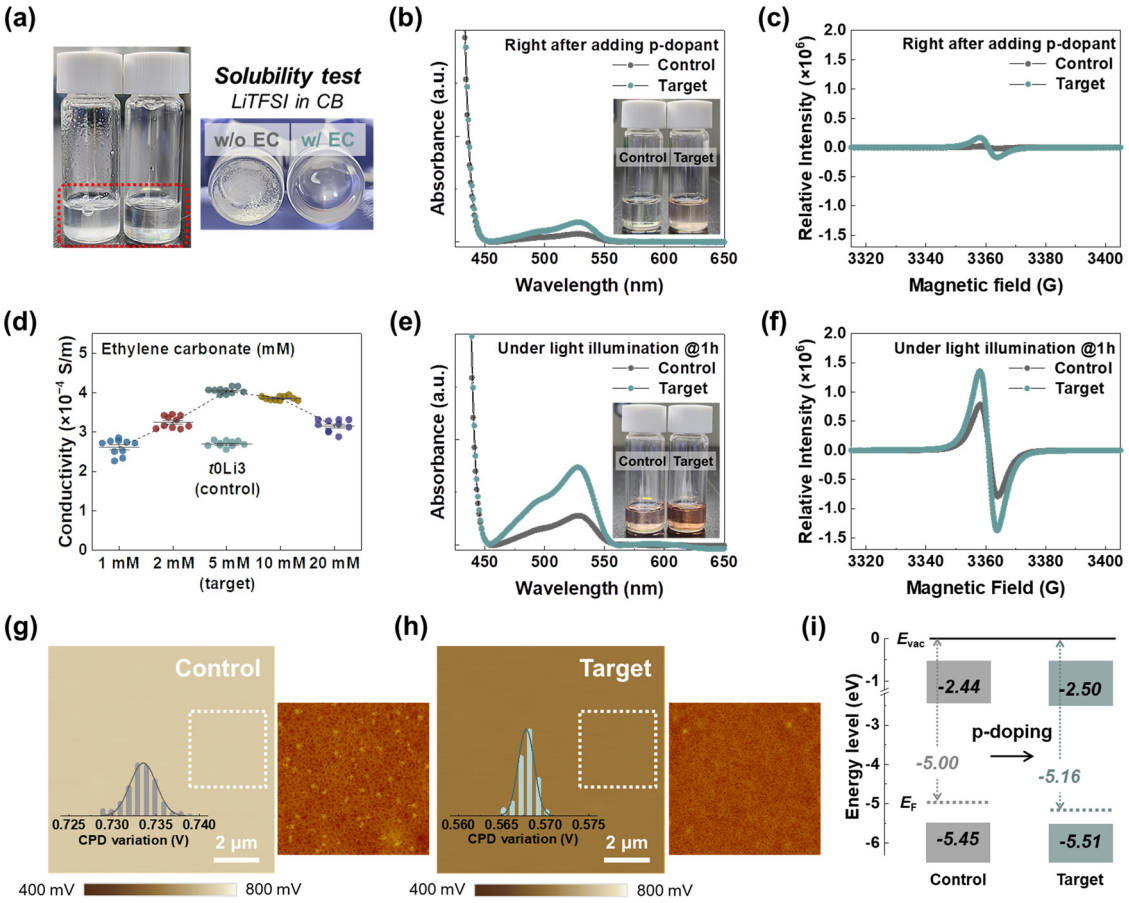

Fig. 2 Electrical properties of EC-incorporated spiro-OMeTAD HTLs. (a) Photographs showing the solubility test of the LiTFSI precursor in the CB solvent without and with the addition of the EC additive. (b) and (c) Absorption and ESR spectra of spiro-OMeTAD solutions, under the control and target conditions, taken immediately after the addition of the LiTFSI dopant. (d) Electrical conductivities of spiro-OMeTAD under different concentrations of the EC additive. (e) and (f) Absorption and ESR spectra of spiro-OMeTAD solutions, under the control and target conditions, after one hour of light illustration. (g) and (h) Surface potential images and distributions of the measured contact potential difference, along with AFM images of spiro-OMeTAD films, under the control and target conditions. (i) Schematic diagram of energy levels of spiro-OMeTAD, under the control and target conditions.

into the electrical conductivity of spiro-OMeTAD films with varying EC concentrations, ranging from 1 mM to 20 mM, while maintaining a LiTFSI of 3 μL (Fig. 2d and Fig. S9, ESI†). The electrical conductivity progressively increased, reaching 4.16×10^{-4} S cm^{-1} at 5 mM of EC (denoted as the target; 0 μL of *t*BP and 3 μL of LiTFSI in 1 mL of CB including 5 mM of EC), beyond which a slight decrease was observed, potentially due to over-doping. The optimal EC concentration of 5 mM corresponds to a 1 : 1 molar ratio with LiTFSI, aligning with theoretical predictions for the strongest binding state under such conditions. The enhanced p-doping under the target conditions was further substantiated by a significantly intensified absorption peak at 520 nm (Fig. 2e), which signifies an increase in doping efficiency from 2.77% to 7.37%[11] following the incorporation of the EC additive, accompanied by a pronounced ESR signal (Fig. 2f).

Beyond its role in improving the solubility of the LiTFSI dopant, *t*BP is widely recognized for improving the miscibility of the spiro-OMeTAD film, promoting its morphological homogeneity.[9,29] As shown in the atomic force microscopy (AFM) images (Fig. S7, ESI†), the exclusion of *t*BP results in undesirable morphological properties, with clearly visible undissolved and aggregated LiTFSI precursors[30] at higher magnification under the control conditions (Fig. 2g). These aggregates act as hole-quenching centres, markedly hindering the feasibility of large-area module applications. The incorporation of the EC additive significantly enhances the solubility of LiTFSI, yielding a homogeneous and smooth spiro-OMeTAD film free from aggregated LiTFSI precursors (Fig. 2h). To further investigate the impact of EC, Kelvin probe force microscopy (KPFM) measurements were conducted on the spiro-OMeTAD film to examine the homogeneity of surface potential. The spiro-OMeTAD film under the target conditions unequivocally revealed a more homogeneous distribution of surface potential with pronounced p-type characteristics, compared to the control conditions (Fig. 2g and h). Ultraviolet photoelectron spectroscopy (UPS) measurements validated the changes in the semiconducting properties of the spiro-OMeTAD film induced by the addition of EC (Fig. 2i and Fig. S10, ESI†). The Fermi level (E_F) under the control conditions was determined to be −5.00 eV, which subsequently shifted to −5.16 eV under the target conditions, accompanied by a narrowed energy gap between E_F and the highest occupied

molecular orbital (HOMO) level. These findings compellingly corroborate the effective p-doping of spiro-OMeTAD through the augmented generation of p-doped radicals, a process facilitated by the introduction of EC, even without *t*BP. Consequently, the electrical properties and energy level alignment achieved through the altered HTL system are favourable for attaining superior efficiency.

Leveraging this advanced HTL system, we evaluated the performance of photovoltaic devices with a fluorine-doped tin oxide (FTO)/tin dioxide (SnO_2)/formamidinium lead iodide ($FAPbI_3$)-based/spiro-OMeTAD/Au configuration (Fig. 3a). Under target conditions, the optimized PSCs achieved a maximum PCE of 25.56% (certified 25.51%, Fig. S11, ESI†), with a short-circuit current density (J_{SC}) of 26.03 mA cm^{-2}, an open-circuit voltage (V_{OC}) of 1.180 V, and a fill-factor (FF) of 83.18%, surpassing the 24.16% obtained under control conditions, and demonstrating noticeable reproducibility with a narrower distribution (Fig. 3b and Fig. S12, and Table S2, ESI†). The integrated J_{SC} value of 25.97 mA cm^{-2} was obtained from external quantum efficiency (EQE) measurements (Fig. S13, ESI†). Notably, the synergetic effects stemming from the incorporation of the EC additive resulted in a pronounced enhancement in V_{OC}, increasing from 1.162 V to 1.180 V. This enhancement is ascribed to the expedited p-doping mechanism within spiro-OMeTAD, mediated by EC, which confers elevated electrical conductivity (Fig. 2d) and an optimal energy level alignment (Fig. 2i). The device under target conditions achieved PCEs of 25.56% and 25.36% in the reverse and forward scans, respectively, with an inconsequential hysteresis index (Fig. 3c). It also attained a stabilized power output (SPO) of 25.44% under standard 1-sun simulated illumination (the inset in Fig. 3c). To the best of our knowledge, the PCE of 25.56% is the highest efficiency thus far reported for *t*BP-free spiro-OMeTAD-based n–i–p PSCs[12,14,31–40] (Fig. 3d and Table S3, ESI†).

The incorporation of the EC additive enhances the morphological uniformity and surface potential of the spiro-OMeTAD film, underscoring its suitability for large-area module applications and potential for scaled-up implementations.[41] To evaluate the feasibility of the proposed approaches for larger-area applications, we fabricated PSMs (aperture area of 25 cm^2) with a configuration of FTO/c-TiO_2/SnO_2/$FAPbI_3$-based/spiro-OMeTAD/Au. The EC-incorporated spiro-OMeTAD system achieved a maximum PCE of 23.22%, along with a geometrical fill factor (GFF) of 94.60% (Fig. 3e and Fig. S14, and Table S4, ESI†). In scaled-up applications, it also demonstrated enhanced reproducibility (Fig. S15, ESI†) and a minimal hysteresis of 0.073 (Fig. S16, ESI†). In a similar vein, we additionally fabricated PSMs with an aperture area of 100 cm^2, which yielded an enhanced PCE of 22.14%, coupled with a GFF of 86.40% and a markedly low hysteresis index of 0.081 (Fig. S14, S16 and Tables S5, S6, ESI†). The certified PCEs of PSMs with aperture areas of 25 and 100 cm^2 were 22.97% and 21.02%, respectively (Fig. S17 and S18, ESI†). Notably, both PSMs exhibited a pronounced enhancement in V_{OC}, affirming the efficacy of the EC-integrated HTL system, even in large-scale devices.

Conventional spiro-OMeTAD-based n–i–p PSCs, which utilize high concentrations of *t*BP and LiTFSI, exhibit a T_g below 85 °C, limiting their compliance with International Summit on Organic Photovoltaics (ISOS-D) stability protocols, particularly under 85 °C/85% RH damp-heat conditions.[42,43] The inclusion of *t*BP markedly diminishes the T_g of spiro-OMeTAD, which otherwise has a T_g of approximately 125 °C in spiro-OMeTAD

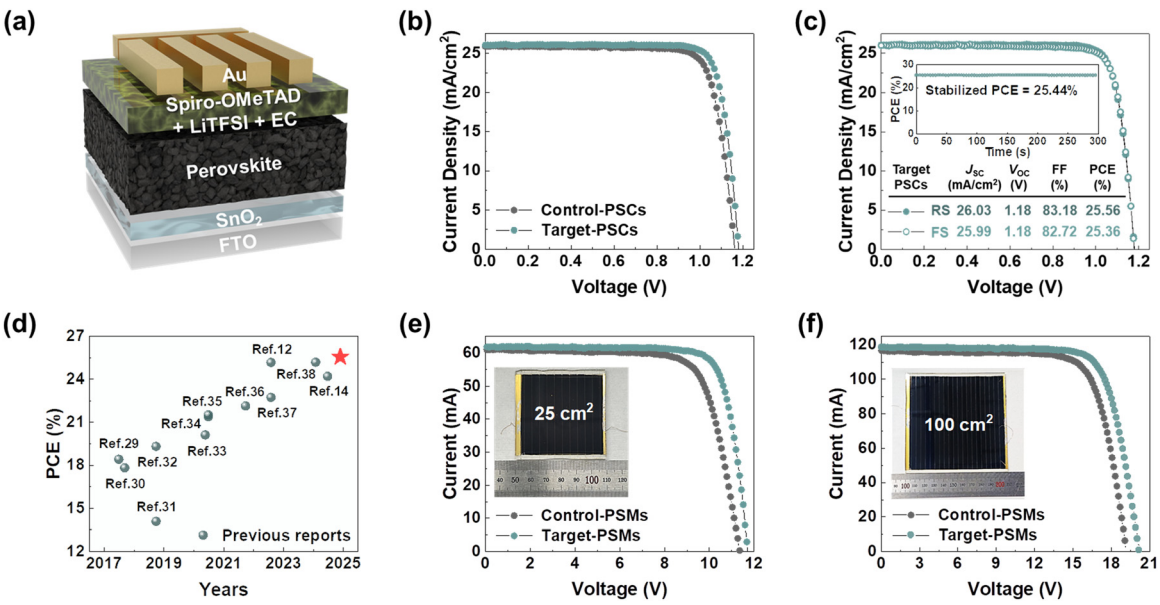

Fig. 3 Photovoltaic performances upon EC-incorporated spiro-OMeTAD HTLs. (a) Configuration of the PSC device structured with the FTO/SnO_2/perovskite/spiro-OMeTAD/Au. (b) *J*–*V* curves of the PSCs under the control and target conditions. (c) *J*–*V* curves and SPO of the PSCs under the target conditions in both reverse and forward scanning directions. (d) Plots showing the PCE values of previously reported PSCs using *t*BP-free spiro-OMeTAD HTLs; detailed parameters are listed in Table S3 (ESI†). (e) and (f) *I*–*V* curves measured with the FTO/c-TiO_2/SnO_2/perovskite/spiro-OMeTAD/Au of the PSMs, with aperture areas of 25 and 100 cm^2, respectively, under the control and target conditions.

without *t*BP, compromising the long-term thermal stability of PSCs. While *t*BP is recognized as a critical factor compromising thermal stability, the *t*BP-free HTL system demonstrates superior thermal resilience, with T_g values exceeding 120 °C under both control and target conditions, as evidenced by the dynamic mechanical analysis (DMA) spectra (Fig. 4a). Under the target conditions, despite the substitution of *t*BP with EC electrolyte, the T_g remains unaffected, underscoring the retention of the intrinsic stability of spiro-OMeTAD while maintaining its structural integrity. Furthermore, this enhancement in the intrinsic stability of spiro-OMeTAD enables the seamless integration of EVA-based encapsulation processing, thereby ensuring the sustained operational integrity of the device under prolonged damp-heat conditions.

Although the exclusion of *t*BP enhances the intrinsic stability of spiro-OMeTAD, the migration of Li^+ and I^- ions, triggered under light and thermal conditions, remains a concern. We examined changes in the electrical conductivity of spiro-OMeTAD under light illumination and thermal stress at 85 °C for 500 hours (Fig. 4b, c and Fig. S19, ESI†). Under control conditions, the electrical conductivity of spiro-OMeTAD decreased to 59.7% of its initial value under light illumination and 71.3% under thermal stress after 500 hours. In contrast, the formation of the Li^+:EC complex constrains the migration of Li^+ ions and their accumulation within the device, effectively preserving the electrical conductivity even after exposure to both conditions. The depth profiling results obtained from time-of-flight secondary ion mass spectrometry (ToF-SIMS) provide a clear elucidation of the ion migration phenomenon. Under the control conditions, it is evident that Li^+ ions exhibit facile migration across the perovskite layer toward the perovskite/ETL interface, even in the absence of external stimuli, corroborating that Li^+ ions are highly susceptible to migration without the presence of the EC (Fig. S20, ESI†). After exposure to both light illumination and thermal stress, a high concentration of Li^+ ions accumulated at the Au/HTL and perovskite/ETL interfaces under control conditions[44,45] (Fig. 4d), while under target conditions, these ions were predominantly localized within the HTL (Fig. 4e). Regarding the thermal stability of the target conditions, molecular simulations revealed that the solvation characteristics of Li^+ ions and EC molecules remained stable (Fig. S21, ESI†). Moreover, the binding strength

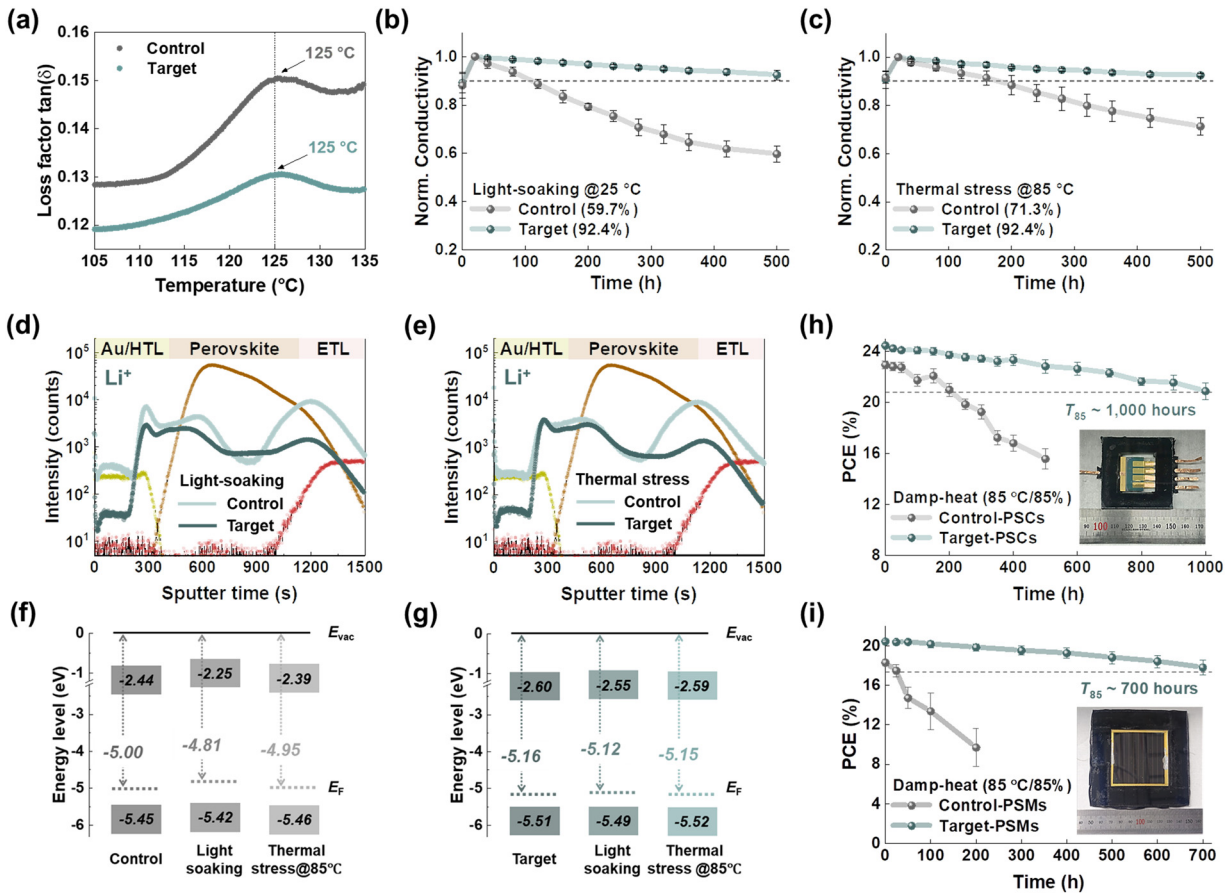

Fig. 4 Durability test upon EC-incorporated spiro-OMeTAD HTLs. (a) DMA graphs of spiro-OMeTAD films under the control and target conditions. (b) and (c) Variation of electrical conductivities measured with the device of FTO/spiro-OMeTAD/Au under light illumination and thermal stress at 85 °C, respectively. (d) and (e) ToF-SIMS depth profiles of Li^+ ions in the device of FTO/SnO_2/perovskite/spiro-OMeTAD/Au. (f) and (g) Schematic diagram of energy levels of spiro-OMeTAD, after being subjected to light illumination and thermal stress at 85 °C for 500 hours. (h) and (i) Damp-heat (85 °C/85% RH) stability of the encapsulated PSCs and PSMs with an aperture area of 25 cm^2, respectively.

between Li^+ ions and EC molecules was maintained at 85 °C (Fig. S22, ESI†), indicating that the migration Li^+ ions can be effectively suppressed by the presence of EC molecules.

For Li^+ ions to accumulate at the perovskite/ETL interface, they must inevitably penetrate the perovskite, a process that induces irreversible phase transformation of α-$FAPbI_3$ and generates significant iodine defects.[46,47] We investigated the effect of Li^+ ion migration on the crystalline stability of the perovskite layer under light illumination and thermal stress and evaluated the ensuing impacts on its structural integrity and phase characteristics (Fig. S23, ESI†). Severe migration of Li^+ ions precipitates structural degradation of the perovskite crystal, evidenced by an increased intensity ratio of the PbI_2 peak compared to that of the (001) crystal. Additionally, subsequent to the removal of both spiro-OMeTAD and the Au electrode, distinct partial degradation or delamination of the perovskite film was observed under control conditions; in contrast, under target conditions, the perovskite film remained intact despite exposure to severe stimuli (Fig. S24 and S25, ESI†). Another issue stemming from the migration of Li^+ ions is the invasion of iodide, which occurs alongside perovskite degradation. The p-doped radicals experience a de-doping process triggered by infiltrated iodide, compromising both electrical properties and interfacial band alignment.[48,49] The E_F of the spiro-OMeTAD film under control conditions was determined to be −5.00 eV, increasing to −4.81 eV and −4.95 eV after exposure to light illumination and thermal stress, respectively (Fig. 4f, g and Fig. S26, ESI†). Under target conditions, the relatively inhibited iodide invasion correlates with a modest increase in E_F from −5.16 eV to −5.12 eV and −5.15 eV, respectively, as further substantiated by ToF-SIMS analysis of I^- ions (Fig. S27, ESI†). The invasion of iodide not only triggers the de-doping of spiro-OMeTAD but also promotes the formation of AuI_2^- *via* the diffusion of Au ions, leading to their subsequent accumulation at the interface. Under control conditions, following exposure to both light illumination and thermal stress at 85 °C, the concentration of AuI_2^- at the Au/HTL interface exhibited a significantly greater increase compared to the target conditions, suggesting a more pronounced formation and accumulation of AuI_2^- at the interface (Fig. S28, ESI†). Furthermore, the diffusion of Au ions can be substantiated through a comparative analysis of the breakdown voltage by applying a reverse bias to the device (Fig. S29, ESI†). Under control conditions, a notable surge in current density was observed at an applied bias of 13.8 V, whereas a considerably higher breakdown voltage of 17.8 V was attained under the target conditions, signifying a restrained diffusion of Au ions into the perovskite layer. It unequivocally validates that the diffusion of Li^+ ions catalysed the deterioration of the critical constituent layer within the devices, instigating the migration of associated ionic species and ultimately undermining the structural and functional integrity of these layers. In conjunction with these experimental and theoretical findings presented herein, the formation of a robust Li^+:EC solvating complex not only elevates the electrical properties of *t*BP-free spiro-OMeTAD systems but also substantially curtails ion migration under intense external stimuli.

Ultimately, with a significantly elevated T_g surpassing at 120 °C and substantially mitigated ion migration, we conducted stability assessments under extended dry heat conditions (85 °C, 15% for low humidity) on encapsulated PSCs (Fig. S30, ESI†). Under the target conditions, PSCs retained over 90% of their initial PCE after 500 hours, whereas those under control conditions exhibited an accelerated degradation, with PCE declining by 78% over the same period. Despite the enhancement in the intrinsic stability of spiro-OMeTAD under both control and target conditions, the pronounced migration of Li^+ ions and pervasive iodide invasion critically compromised the electrical properties of the charge transporting layer under thermal stress, ultimately precipitating severe efficiency losses in control-PSCs. Leveraging the exceptional thermal resilience of target-PSCs, we extended our investigation to PSCs and large-area PSMs with EVA-based encapsulation, subjecting them to prolonged damp-heat conditions (85 °C/85% RH) to evaluate the commercial viability of this strategy. For PSCs, under control conditions, the PCE rapidly declined by 68% after 500 hours, whereas the PSCs under the target conditions maintained over 85% of their initial PCE after 1000 hours (Fig. 4h and Fig. S31, ESI†). Similarly, PSMs under control conditions exhibited a 47% reduction in PCE after 200 hours, while those under target conditions preserved over 87% of their initial PCEs even after 700 hours (Fig. 4i and Fig. S32, ESI†). Additionally, under maximum power point tracking (MPPT) conditions (Fig. S33, ESI†), PSCs under control conditions experienced severe degradation, with PCE dropping to 70% after 200 hours at 60 °C. In contrast, PSCs under target conditions retained over 85% of their initial PCE after 500 hours. At an elevated temperature of 85 °C, a pronounced degradation in PCE was observed. Nevertheless, under the target conditions, the PSCs retained over 80% of their initial PCE for 500 hours. Consequently, our proposed strategy provides a crucial framework for attaining durable thermal stability, a persistent and formidable challenge that has persistently impeded advancements in spiro-OMeTAD based n–i–p PSC fields.

Conclusions

We presented a groundbreaking *t*BP-free HTL system by substituting EC electrolyte for *t*BP. The exceptional solvating capability of EC enhances LiTFSI solubility in CB, fostering a morphologically uniform spiro-OMeTAD film free of pinholes and aggregation. This solubility enhancement promotes a higher density of p-doped radicals, thereby improving the electrical properties of spiro-OMeTAD. The resulting PSCs achieved an unprecedented maximum PCE of 25.56% (certified 25.51%), while large-area PSMs attained PCEs of 23.22% and 22.14% with aperture areas of 25 and 100 cm^2, respectively. The elevated T_g and robust Li^+:EC complex led to outstanding reliability, retaining 85% and 87% of their initial efficiency after 1000 and 700 hours for PSCs and PSMs, respectively, under damp-heat conditions (85 °C/85% RH). These findings highlight the profound efficacy of the *t*BP-free HTL protocol in catalysing substantial advancements in both the efficiency and

long-term durability of PSCs, positioning it as a pivotal innovation in the field.

Author contributions

Y. S. S. and D. S. K. conceived the project and designed the experiments. T. K. L. and D. S. K. supervised the work. Y. S. S., D. G. L., T. K. L., and D. S. K. wrote the manuscript. J. L. fabricated the PSMs and performed their long-term damp-heat stability measurements. D. G. L. and T. K. L. carried out molecular simulations (*i.e.*, DFT calculations and MD simulations) and data analysis. J. W. S. fabricated the PSCs and performed their long-term damp-heat stability measurements. J. S. conducted NMR and FT-IR measurements and data analysis. J. R. conducted UPS measurements and data analysis. M. J. S. fabricated the PSCs and performed their long-term operating stability measurements. S. P. and S. C. conducted KPFM measurements and data analysis. G. Y. S. and G.-H. K. conducted DMA measurement and data analysis. J. Y. conducted AFM measurements and data analysis. D. L. conducted an analysis of the electrical properties of spiro-OMeTAD films. C. H. Y. conducted ESR measurements and data analysis. M. K. conducted UV-vis absorption and PL measurements and data analysis. J. G. S. conducted XRD measurements and data analysis. J. Y. K. suggested additional experiments and offered feedback. All authors discussed the results and contributed to the final manuscript.

Data availability

The data supporting this article have been included as part of the ESI.†

Conflicts of interest

There are no conflicts to declare.

Acknowledgements

This work was supported by the National Research Foundation of Korea (NRF) grant funded by the Korean government (MSIT) (NRF-2023R1A2C3007358). This work was supported by the Korea Institute of Energy Technology Evaluation and Planning (KETEP) and the Ministry of Trade, Industry & Energy (MOTIE) of the Republic of Korea (RS-2024-00457537). This work was supported by Learning & Academic research institution for Masters, PhD students, and Postdocs (LAMP) Program of the NRF grand funded by the Ministry of Education (No. RS-2023-00301974). This work was supported by the Basic Science Research Program through the NRF funded by the Ministry of Education (RS-2024-00459908).

Notes and references

1 J.-Y. Seo, H.-S. Kim, S. Akin, M. Stojanovic, E. Simon, M. Fleischer, A. Hagfeldt, S. M. Zakeeruddin and M. Grätzel, *Energy Environ. Sci.*, 2018, **11**, 2985–2992.
2 J. Burschka, A. Dualeh, F. Kessler, E. Baranoff, N.-L. Cevey-Ha, C. Yi, M. K. Nazeeruddin and M. Grätzel, *J. Am. Chem. Soc.*, 2011, **133**, 18042–18045.
3 H.-S. Kim, C.-R. Lee, J.-H. Im, K.-B. Lee, T. Moehl, A. Marchioro, S.-J. Moon, R. Humphry-Baker, J.-H. Yum, J. E. Moser, M. Grätzel and N.-G. Park, *Sci. Rep.*, 2012, **2**, 591.
4 U. B. Cappel, T. Daeneke and U. Bach, *Nano Lett.*, 2012, **12**, 4925–4931.
5 Z. Hawash, L. K. Ono and Y. Qi, *Adv. Mater. Interfaces*, 2016, **3**, 1600117.
6 A. Abate, T. Leijtens, S. Pathak, J. Teuscher, R. Avolio, M. E. Errico, J. Kirkpatrik, J. M. Ball, P. Docampo, I. McPherson and H. J. Snaith, *Phys. Chem. Chem. Phys.*, 2013, **15**, 2572–2579.
7 S. Wang, M. Sina, P. Parikh, T. Uekert, B. Shahbazian, A. Devaraj and Y. S. Meng, *Nano Lett.*, 2016, **16**, 5594–5600.
8 T. Malinauskas, D. Tomkute-Luksiene, R. Sens, M. Daskeviciene, R. Send, H. Wonneberger, V. Jankauskas, I. Bruder and V. Getautis, *ACS Appl. Mater. Interfaces*, 2015, **7**, 11107–11116.
9 F. Lamberti, T. Gatti, E. Cescon, R. Sorrentino, A. Rizzo, E. Menna, G. Meneghesso, M. Meneghetti, A. Petrozza and L. Franco, *Chem*, 2019, **5**, 1806–1817.
10 A. K. Jena, Y. Numata, M. Ikegami and T. Miyasaka, *J. Mater. Chem. A*, 2018, **6**, 2219–2230.
11 Y. S. Shin, J. W. Song, D. G. Lee, J. Lee, J. Seo, J. Roe, G. Y. Shin, D. Kim, J. Yeop, D. Lee, M. Kim, Y. Jo, H. Jang, J. G. Son, W. Lee, J. Son, S. Park, S. Cho, T. J. Shin, G.-H. Kim, J. Y. Kim, T. K. Lee, M. Grätzel and D. S. Kim, *Joule*, 2025, **9**, 101779.
12 T. Zhang, F. Wang, H.-B. Kim, I.-W. Choi, C. Wang, E. Cho, R. Konefal, Y. Puttisong, K. Terado, L. Kobera, M. Chen, M. Yang, S. Bai, B. Yang, J. Suo, S.-C. Yang, X. Liu, F. Fu, H. Yoshida, W. M. Chen, J. Brus, V. Coropceanu, A. Hagfeldt, J.-L. Brédas, M. Fahlman, D. S. Kim, Z. Hu and F. Gao, *Science*, 2022, **377**, 495–501.
13 J. Kong, Y. Shin, J. A. Röhr, H. Wang, J. Meng, Y. Wu, A. Katzenberg, G. Kim, D. Y. Kim, T.-D. Li, E. Chau, F. Antonio, T. Siboonruang, S. Kwon, K. Lee, J. R. Kim, M. A. Modestino, H. Wang and A. D. Taylor, *Nature*, 2021, **594**, 51–56.
14 M. J. Grotevent, Y. Lu, T. Šverko, M.-C. Shih, S. Tan, H. Zhu, T. Dang, J. K. Mwaura, R. Swartwout, F. Beiglböck, L. Kothe, V. Bulović and M. G. Bawendi, *Adv. Energy Mater.*, 2024, **14**, 2400456.
15 V. Nilsson, A. Kotronia, M. Lacey, K. Edström and P. Johansson, *ACS Appl. Energy Mater.*, 2020, **3**, 200–207.
16 Z. Li, L. Wang, X. Huang and X. He, *Adv. Funct. Mater.*, 2024, 2408319n/a.
17 O. Borodin and G. D. Smith, *J. Phys. Chem. B*, 2006, **110**, 4971–4977.
18 W. Cui, Y. Lansac, H. Lee, S.-T. Hong and Y. H. Jang, *Phys. Chem. Chem. Phys.*, 2016, **18**, 23607–23612.
19 G. Hilmersson, P. I. Arvidsson, Ö. Davidsson and M. Håkansson, *J. Am. Chem. Soc.*, 1998, **120**, 8143–8149.
20 W. Bauer and P. V. R. Schleyer, *Magn. Reson. Chem.*, 1988, **26**, 827–833.

21 Y.-Q. Wang, H. Xu, B. Cao, J. Ma and Z.-W. Yu, *J. Phys. Chem. Lett.*, 2024, **15**, 5047–5055.
22 Y. Chen, Q. He, Y. Zhao, W. Zhou, P. Xiao, P. Gao, N. Tavajohi, J. Tu, B. Li, X. He, L. Xing, X. Fan and J. Liu, *Nat. Commun.*, 2023, **14**, 8326.
23 X. Ye, J. Liang, B. Du, Y. Li, X. Ren, D. Wu, X. Ouyang, Q. Zhang and J. Liu, *Energy Environ. Mater.*, 2024, **7**, e12751.
24 B. Tan, S. R. Raga, A. S. R. Chesman, S. O. Fürer, F. Zheng, D. P. McMeekin, L. Jiang, W. Mao, X. Lin, X. Wen, J. Lu, Y.-B. Cheng and U. Bach, *Adv. Energy Mater.*, 2019, **9**, 1901519.
25 X. Liu, B. Zheng, L. Shi, S. Zhou, J. Xu, Z. Liu, J. S. Yun, E. Choi, M. Zhang, Y. Lv, W.-H. Zhang, J. Huang, C. Li, K. Sun, J. Seidel, M. He, J. Peng, X. Hao and M. Green, *Nat. Photonics*, 2023, **17**, 96–105.
26 M. L. Tietze, P. Pahner, K. Schmidt, K. Leo and B. Lüssem, *Adv. Funct. Mater.*, 2015, **25**, 2701–2707.
27 S. Olthof, S. Mehraeen, S. K. Mohapatra, S. Barlow, V. Coropceanu, J.-L. Brédas, S. R. Marder and A. Kahn, *Phys. Rev. Lett.*, 2012, **109**, 176601.
28 L. K. Ono, Z. Hawash, E. J. Juarez-Perez, L. Qiu, Y. Jiang and Y. Qi, *J. Phys. D: Appl. Phys.*, 2018, **51**, 294001.
29 S. N. Habisreutinger, N. K. Noel, H. J. Snaith and R. J. Nicholas, *Adv. Energy Mater.*, 2017, **7**, 1601079.
30 E. J. Juarez-Perez, M. R. Leyden, S. Wang, L. K. Ono, Z. Hawash and Y. Qi, *Chem. Mater.*, 2016, **28**, 5702–5709.
31 J. Zhang, T. Zhang, L. Jiang, U. Bach and Y.-B. Cheng, *ACS Energy Lett.*, 2018, **3**, 1677–1682.
32 A. Pellaroque, N. K. Noel, S. N. Habisreutinger, Y. Zhang, S. Barlow, S. R. Marder and H. J. Snaith, *ACS Energy Lett.*, 2017, **2**, 2044–2050.
33 L. Caliò, M. Salado, S. Kazim and S. Ahmad, *Joule*, 2018, **2**, 1800–1815.
34 J. Zhang, Q. Daniel, T. Zhang, X. Wen, B. Xu, L. Sun, U. Bach and Y.-B. Cheng, *ACS Nano*, 2018, **12**, 10452–10462.
35 J. Liu, W. Liu, E. Aydin, G. T. Harrison, F. H. Isikgor, X. Yang, A. S. Subbiah and S. De Wolf, *ACS Appl. Mater. Interfaces*, 2020, **12**, 23874–23884.
36 G. Sathiyan, A. A. Syed, C. Chen, C. Wu, L. Tao, X. Ding, Y. Miao, G. Li, M. Cheng and L. Ding, *Nano Energy*, 2020, **72**, 104673.
37 Q. Du, Z. Shen, C. Chen, F. Li, M. Jin, H. Li, C. Dong, J. Zheng, M. Ji and M. Wang, *Sol. RRL*, 2021, **5**, 2100622.
38 Y. Dong, J. Zhang, Y. Yang, J. Wang, B. Hu, W. Wang, W. Cao, S. Gai, D. Xia, K. Lin and R. Fan, *Nano Energy*, 2022, **97**, 107184.
39 J. Xia, Y. Zhang, C. Xiao, K. G. Brooks, M. Chen, J. Luo, H. Yang, N. I. D. Klipfel, J. Zou, Y. Shi, X. Yao, J. Chen, J. M. Luther, H. Lin, A. M. Asiri, C. Jia and M. K. Nazeeruddin, *Joule*, 2022, **6**, 1689–1709.
40 H. Yang, T. Xu, W. Chen, Y. Wu, X. Guo, Y. Shen, C. Ding, X. Chen, H. Chen, J. Ding, X. Wu, G. Zeng, Z. Zhang, Y. Li and Y. Li, *Angew. Chem., Int. Ed.*, 2024, **63**, e202316183.
41 F. M. Rombach, S. A. Haque and T. J. Macdonald, *Energy Environ. Sci.*, 2021, **14**, 5161–5190.
42 R. Cheacharoen, C. C. Boyd, G. F. Burkhard, T. Leijtens, J. A. Raiford, K. A. Bush, S. F. Bent and M. D. McGehee, *Sustainable Energy Fuels*, 2018, **2**, 2398–2406.
43 H. Kim, J. Sin, M. Kim, G. Kim, M. Kim, J. Kim, G. Park, B. Kim, M. S. Jeong and J. Yang, *Sol. RRL*, 2024, **8**, 2300825.
44 S.-G. Kim, T. H. Le, T. de Monfreid, F. Goubard, T.-T. Bui and N.-G. Park, *Adv. Mater.*, 2021, **33**, 2007431.
45 Z. Li, C. Xiao, Y. Yang, S. P. Harvey, D. H. Kim, J. A. Christians, M. Yang, P. Schulz, S. U. Nanayakkara, C.-S. Jiang, J. M. Luther, J. J. Berry, M. C. Beard, M. M. Al-Jassim and K. Zhu, *Energy Environ. Sci.*, 2017, **10**, 1234–1242.
46 S.-G. Choi and J.-W. Lee, *EcoMat*, 2023, **5**, e12398.
47 J. A. Dawson, A. J. Naylor, C. Eames, M. Roberts, W. Zhang, H. J. Snaith, P. G. Bruce and M. S. Islam, *ACS Energy Lett.*, 2017, **2**, 1818–1824.
48 T. Zhang, X. Meng, Y. Bai, S. Xiao, C. Hu, Y. Yang, H. Chen and S. Yang, *J. Mater. Chem. A*, 2017, **5**, 1103–1111.
49 T. Wang, Y. Zhang, W. Kong, L. Qiao, B. Peng, Z. Shen, Q. Han, H. Chen, Z. Yuan, R. Zheng and X. Yang, *Science*, 2022, **377**, 1227–1232.